

# Design and Beam Test Results for the 2D Projective sPHENIX Electromagnetic Calorimeter Prototype

C.A. Aidala, S. Altaf, R. Belmont, S. Boose, D. Cacace, M. Connors, E. Desmond, J. Frantz, E.A. Gamez, N. Grau, J.S. Haggerty, A. Hodges, J. Huang, Y. Kim, M.D. Lenz, W. Lenz, N.A. Lewis, E.J. Mannel, J.D. Osborn, D.V. Perepelitsa, M. Phipps, R. Pisani, S. Polizzo, A. Pun, M.L. Purschke, C. Riedl, T. Rinn, A.C. Romero Hernandez, M. Sarsour, Z. Shi, A.M. Sickles, C. Smith, S. Stoll, X. Sun, E. Thorsland, F. Vassalli, X. Wang, C.L. Woody

**Abstract**—sPHENIX is a new experiment under construction for the Relativistic Heavy Ion Collider at Brookhaven National Laboratory which will study the quark-gluon plasma to further the understanding of QCD matter and interactions. A prototype of the sPHENIX electromagnetic calorimeter (EMCal) was tested at the Fermilab Test Beam Facility in Spring 2018 as experiment T-1044. The EMCal prototype corresponds to a solid angle of  $\Delta\eta \times \Delta\phi = 0.2 \times 0.2$  centered at pseudo-rapidity  $\eta = 1$ . The prototype consists of scintillating fibers embedded in a mix of tungsten powder and epoxy. The fibers project back approximately to the center of the sPHENIX detector, giving 2D projectivity. The energy response of the EMCal prototype was studied as a function of position and input energy. The energy resolution of the EMCal prototype was obtained after applying a position dependent energy correction and a beam profile correction. Two separate position dependent corrections were considered. The EMCal energy resolution was found to be  $\sigma(E)/\langle E \rangle = 3.5(0.1) \oplus 13.3(0.2)/\sqrt{E}$  based on the hodoscope position dependent correction, and  $\sigma(E)/\langle E \rangle = 3.0(0.1) \oplus 15.4(0.3)/\sqrt{E}$  based on the cluster position dependent correction. These energy resolution results meet the requirements of the sPHENIX physics program.

**Index Terms**—Calorimeters, electromagnetic calorimetry, performance evaluation, prototypes, Relativistic Heavy Ion Collider (RHIC), silicon photomultiplier (SiPM), simulation, “Spaghetti” Calorimeter (SPACAL), sPHENIX

## I. INTRODUCTION

sPHENIX is a new experiment [1] under construction for the Relativistic Heavy Ion Collider at Brookhaven National Laboratory which will study the quark-gluon plasma (QGP) [2]–[6] to further the understanding of QCD matter and interactions. sPHENIX is designed to measure the QGP at a variety of length scales using various probes to provide insights into the microscopic properties of the QGP. One such probe is jets that arise from hard scattering interactions between two partons, with the energy loss of partons traversing the QGP being of particular interest. sPHENIX will allow for a detailed study of flavor dependent energy loss through a measurement of heavy flavor tagged jets, as well as open heavy flavor hadrons. Measurements of photon-tagged jets and jet substructure are also part of the sPHENIX physics program. sPHENIX will allow for measurements of jets with transverse momentum as low as 10 GeV, as well as provide measurements of both the hadronic and electromagnetic components of jets at RHIC. To

accomplish these measurements, sPHENIX is designed with a tracking system, a calorimeter system with  $2\pi$  azimuthal acceptance and pseudorapidity coverage of  $|\eta| < 1.1$ , and the former BaBar solenoid magnet [7]. The calorimeter system consists of an electromagnetic calorimeter and a hadronic calorimeter. The use of the BaBar magnet imposed constraints on the sPHENIX detector design. In particular, the electromagnetic calorimeter was required to be compact enough to fit inside the magnet while allowing enough space for the tracking system and part of the hadronic calorimeter. The electromagnetic calorimeter was also designed to be compact in order to minimize the cost of the calorimeter system.

The sPHENIX electromagnetic calorimeter (EMCal) is a sampling calorimeter designed to measure the electrons, positrons, and photons in electromagnetic showers. The EMCal will also measure approximately one interaction length of hadronic showers. The EMCal has a coverage of  $|\eta| < 1.1$  and full azimuth. The EMCal is segmented into *towers* of size  $\Delta\eta \times \Delta\phi = 0.024 \times 0.024$ , with an approximate volume of  $2.5 \times 2.5 \times 14 \text{ cm}^3$ , which sets the granularity of the calorimeter. The towers are defined within calorimeter *blocks* that consist of scintillating fibers embedded in a mix of tungsten powder and epoxy. Each block corresponds to a  $2 \times 2$  array of towers. Each tower is equipped with a *light guide* coupled to silicon photomultipliers that collect the light from the fibers. The blocks are distributed in 64 sectors that describe an overall cylindrical geometry concentric with the beamline and centered at the interaction point of the particle collisions. Each side  $0 < |\eta| < 1.1$  has 32 sectors distributed evenly in azimuth. Each sector has 24 rows of blocks extending along the beamline, and each row has 4 blocks along the  $\phi$  direction. The blocks are tapered in both  $\eta$  and  $\phi$ , resembling a truncated pyramid, and giving a 2D projective geometry. The blocks are further tilted such that the fibers do not project directly at the interaction point, minimizing channeling and improving energy resolution. More details about the sPHENIX detector and the EMCal can be found in reference [8].

The sPHENIX physics program requires an EMCal energy resolution equal or better than  $16\%/\sqrt{E} \oplus 5\%$ . This requirement is motivated by the measurement of the Upsilon states through the electronic decay channel  $\Upsilon \rightarrow e^-e^+$ . The electrons from these Upsilon decays are expected to produce EMCal electromagnetic showers with energies of approximately 4 to 10 GeV. In contrast, underlying event fluctuations

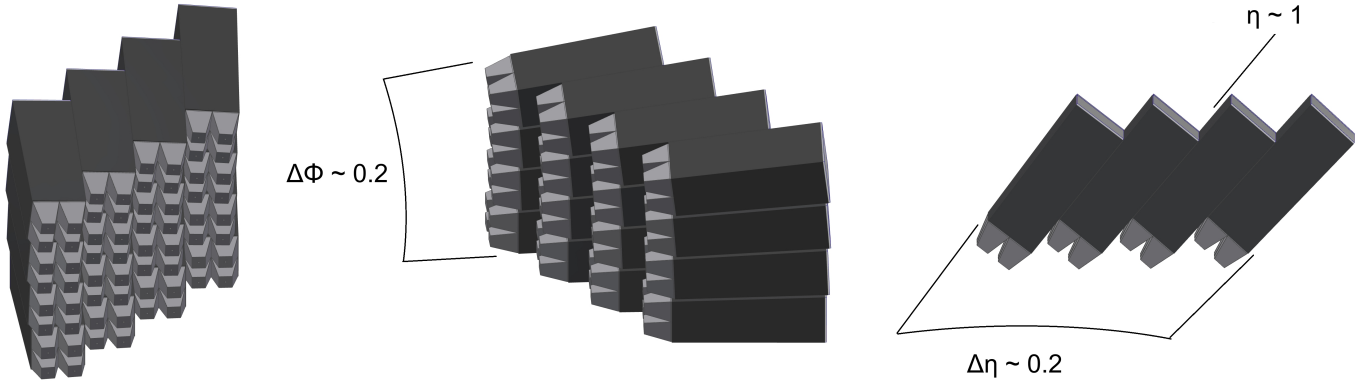


Fig. 1. EMCAL prototype. The prototype consists of an array of  $4 \times 4$  blocks, covering a solid angle of  $\Delta\eta \times \Delta\phi = 0.2 \times 0.2$  centered at  $\eta = 1$ . Each block (dark gray) corresponds to a  $2 \times 2$  array of towers defined by light guides (light gray).

in central Au+Au collisions would produce a comparable measurement of approximately 320 MeV [8]. The energy resolution requirement was based on the maximum energy smearing that would allow discrimination of the Upsilon states against the average underlying event fluctuations.

A prototype of the EMCAL was constructed in order to test its energy resolution. The prototype corresponded to an array of  $8 \times 8$  calorimeter towers, or  $4 \times 4$  blocks, centered at  $\eta = 1$ . The prototype covered a solid angle of  $\Delta\eta \times \Delta\phi = 0.2 \times 0.2$ . Figure 1 shows a schematic view of the EMCAL prototype.

A previous prototype of the EMCAL was tested in 2016 [9]. There are various differences between the 2016 prototype and the 2018 prototype discussed in this paper. The most notable difference is the projectivity of the EMCAL blocks. The 2016 prototype was only 1D projective (in  $\phi$ ), whereas the 2018 prototype is 2D projective (in  $\eta$  and  $\phi$ ). The 2D projectivity is a desirable feature because it improves energy measurements at higher pseudorapidity. For a 2D projective design, an electromagnetic shower at high pseudorapidity is contained within a smaller number of towers than for a 1D design, which results in a greater signal per tower and a better discrimination against underlying event fluctuations. Another difference between the prototypes is the pseudorapidity region that they covered. While both prototypes corresponded to a slice  $\Delta\eta \times \Delta\phi = 0.2 \times 0.2$  of the EMCAL, the 2016 prototype was centered at  $\eta = 0$  and the 2018 prototype was centered at  $\eta = 1$ . The change in pseudorapidity was motivated by the fact that the 2D projectivity reduces to 1D towards  $\eta = 0$  because the sPHENIX detector is symmetric with respect to this plane. Other changes were also introduced in the 2018 prototype in order to optimize the EMCAL design (details in reference [8]), but the 2D projectivity and the high pseudorapidity are the main differences with respect to the previous prototype. The final EMCAL design that will be implemented in sPHENIX will closely follow the design of the 2018 prototype.

## II. PROTOTYPE ELECTROMAGNETIC CALORIMETER

### A. EMCAL Block Production

The EMCAL blocks were produced by embedding a matrix of scintillating fibers in a mix of epoxy and tungsten powder. The blocks are similar to the ‘‘Spaghetti Calorimeter’’ design

used in other experiments [10]–[16]. The scintillating fibers are as long as the block and are distributed uniformly across the block’s cross section. There is a total of 2668 fibers per block. The towers within a block have an area of approximately  $(1.1R_M)^2$ , where  $R_M \approx 2.3$  cm is the Molière radius. The length of the towers varies with  $\eta$  and it has an approximate value of  $20X_0$ , where  $X_0 \approx 7$  mm is the radiation length. The block density is approximately  $9.5$  g/cm<sup>3</sup>, with a sampling fraction of approximately 2.1%.

TABLE I  
EMCAL BLOCK MATERIALS

Material	Property	Value
Scintillating fiber	Saint Gobain BCF-12 diameter	0.47 mm
	core material	polystyrene
	cladding material	acrylic
	cladding	single
	emission peak	435 nm
	decay time	3.2 ns
	attenuation length	$\geq 1.6$ m
Tungsten powder	THP Technon 100 mesh particle size	25-150 $\mu$ m
	bulk density (solid)	$\geq 18.50$ g/cm <sup>3</sup>
	tap density (powder)	$\geq 10.9$ g/cm <sup>3</sup>
	purity	$\geq 99\%$ W
	impurities ( $\leq 1\%$ )	Fe, Ni, O <sub>2</sub> , Co, Cr, Cu, Mo
Epoxy	EPO-TEK 301	

The materials used to produce the blocks are listed in Table I along with some of their properties. The blocks were produced at the University of Illinois at Urbana-Champaign following this procedure [8]:

- Scintillating fibers are dropped into mesh screens that hold the fibers in place.
- The fiber-screen assembly is put into a mold.
- Tungsten powder is poured into the mold. The mold is placed on a vibrating table to pack the powder.
- Epoxy is poured into the top of the filled mold, while a vacuum pump is used at the bottom to extract the air as well as pull the epoxy through the mold.
- The filled mold is left to dry until the mix is solid.

- The block is unmolded and machined to its final shape. A diamond tip is used to machine the readout ends of the block.

A finished EMCal block can be seen in Figure 2. The quality assurance of the blocks included tests of density, light transmission and size. The blocks had a density ranging from 9.2 to 9.8 g/cm<sup>3</sup>. All the blocks had more than 99% fibers that successfully transmitted light. The size of the blocks deviated from the nominal dimensions by less than 0.5 mm.

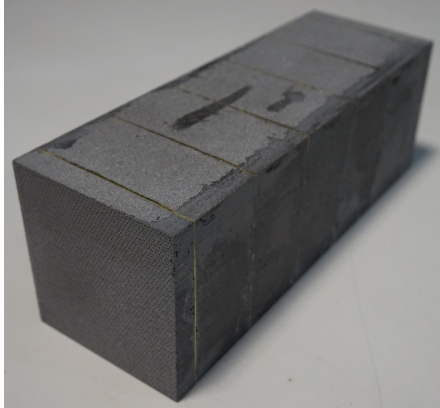


Fig. 2. EMCal block. The block consists of scintillating fibers embedded in a mix of tungsten powder and epoxy. The blocks are tapered in two dimensions, giving a 2D projective geometry.

### B. Light Collection

The light from the scintillating fibers was collected at the tower's front end (closer to the interaction point). Light guides were epoxied to the front of the blocks, while aluminum reflectors were epoxied to the back. The light guides consisted of UV transmitting acrylic with a trapezoidal shape (see Figure 3), custom made by NN, Inc.<sup>1</sup> A silicone adhesive was used to couple each light guide to a 2×2 array of silicon photomultipliers (SiPM). Each SiPM (Hamamatsu S12572-015P) had an active area of 3×3 mm<sup>2</sup> containing 40K 15μm pixels, and had a photon detection efficiency of 25%. The signals from each of the four SiPMs were summed to give a single output signal from each tower. More details about the electronics are given in Section III. Figure 3 shows an EMCal block equipped with light guides and SiPMs.

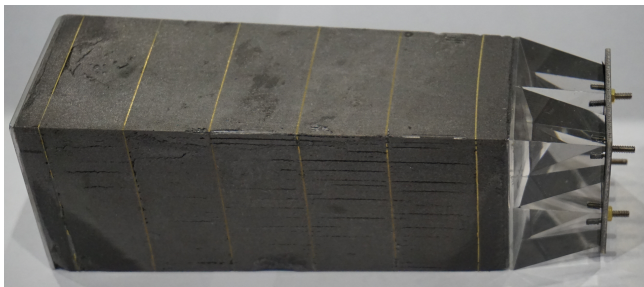


Fig. 3. EMCal block equipped with light guides and SiPMs.

<sup>1</sup>NN, Inc., Precision Engineered Products Group, East Providence, RI 02914.

### C. Assembly

Once the EMCal blocks were equipped with light guides and SiPMs, they were stacked and epoxied together in their final positions. Since the SiPM gain is sensitive to temperature, a cooling system was used to remove the heat generated by the electronics. The cooling system consisted of multiple water coils connected to cold plates. The plates were coupled to the preamplifier boards that follow the SiPMs. Both the cooling system and electronics were controlled remotely. The EMCal prototype can be seen in Figure 4, which shows the blocks, light guides, SiPMs, electronics and part of the cooling system.

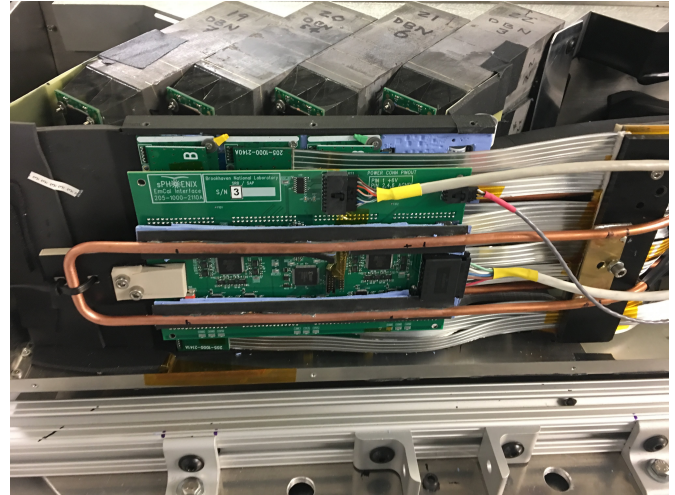


Fig. 4. EMCal prototype showing the EMCal blocks, light guides, SiPMs, electronics and part of the cooling system.

### III. READOUT ELECTRONICS AND DATA ACQUISITION

The summed signals from the four SiPMs from a tower were sent to a preamplifier, then shaped and driven into a digitizer. The SiPMs were operated at 4V above their breakdown voltage, which produces a gain of approximately  $2.3 \times 10^5$ . A small thermistor was mounted at the center of the four SiPMs to monitor the temperature per tower. The temperature of the SiPMs was held constant within approximately 0.5°C. Since the gain temperature dependence of the SiPMs is approximately 1.5%/°C, temperature variations did not contribute significantly to the measured energy resolution. LEDs with an emission peak at 405 nm were mounted near the readout end of each tower and were used to provide a pulsed light source for calibration. Similarly, a charge injection test pulse was used to test and calibrate the readout electronics. The EMCal prototype could operate in a nominal gain mode, or a high gain mode with 16 times the normal gain. The gain was selected through a slow control system.

The slow control system consisted of an interface board connected to a controller board. The interface board was mounted on the EMCal prototype while the controller board was in a separate crate. The interface board contained digital-to-analog converters needed for different testing and monitoring tasks. The interface board controlled the SiPM bias and gain. Testing of the preamplifiers was controlled through the interface board



as well. The interface board also monitored leakage current and local temperature for compensation. The parameters for these testing and monitoring tasks were provided to the interface board by the controller board. An ethernet connection was used to communicate with the controller board.

Signals were digitized using a digitization system developed for PHENIX [17]. The signal waveforms were digitized using Analog-to-digital converters (ADC) at a sampling frequency of 60 MHz, followed by Field Programmable Gate Arrays. Signals were collected in Data Collection Modules and the data was finally recorded using the data acquisition system RCDAQ [18], [19]. The signals were recorded for the EMCal prototype as well as the external detectors mentioned in section IV.

#### IV. TEST BEAM

The EMCal prototype was tested at the Fermilab Test Beam Facility as experiment T-1044. The facility provided a particle beam, detectors such as a lead-glass calorimeter and Cherenkov counters, and a motion table in the MT6.2C area [20]. The EMCal was placed on the motion table to allow testing in different positions with respect to the beam.

The particle beam used in the experiment had energies ranging from 2 to 28 GeV and a profile size of a few centimeters, dependent on beam energy. The beam was composed mainly of electrons, muons, and pions, and their relative abundance depended on the energy [21], [22]. The beam hit the EMCal prototype with a frequency of 1 spill per min, where a spill corresponds to a maximum of approximately  $10^5$  particles during 4 seconds. The beam had a nominal momentum spread of  $\delta p/p \approx 2\%$  for the energy range used [9], [10], [23]. A lead-glass calorimeter was used to measure the average and the spread of the beam momentum. The lead-glass calorimeter had a size of  $45 \times 15 \times 15 \text{ cm}^3$  and an approximate resolution of  $1.4\% \oplus 5.0\%/\sqrt{E}$  [9].

External detectors were used to discriminate electron signals from minimum ionizing particles (MIPs) and hadrons. Two gaseous Cherenkov counters were used for particle identification. The gas pressure in each Cherenkov counter was tuned to trigger only on electron signals. A hodoscope [10], [11] was placed upstream of the EMCal to determine the position of the particles in the beam precisely. The hodoscope consisted of 16 hodoscope fingers (0.5 cm wide scintillators) arranged in two arrays of 8 fingers each. One array had the hodoscope fingers arranged vertically and the other array had them arranged horizontally. The position of a hit in the hodoscope was given by a horizontal and a vertical hodoscope channel number. Each hodoscope finger was read out by an SiPM. Four veto detectors were also placed around the EMCal in order to suppress particles traveling outside the acceptance of the hodoscope. Each veto counter consisted of a scintillator coupled to a photomultiplier tube (PMT).

#### V. SIMULATIONS

The EMCal prototype was simulated using GEANT4 [24], [25] version 4.10.02-patch-02, with the physics list QGSP\_BERT. The EMCal blocks were simulated following

their nominal design with a uniform block density. The simulations included an electron beam with a Gaussian profile. An 8 GeV beam with a standard deviation of 8 cm was used to study the prototype's energy response as a function of position. To study the prototype's energy response as a function of energy, the beam had an energy between 2 and 28 GeV and a standard deviation of 2.5 cm. For this energy dependent study, the beam was pointed between Towers A and B, which are located near the center of the prototype (see Figure 5). In the simulations, the energy deposits from the electromagnetic showers were converted into light using Birks' law [26] with constant  $k_B = 0.0794 \text{ mm/MeV}$  [27]. The number of photons collected was reduced by the light guide collection efficiency and then converted to number of fired SiPM pixels taking into account the SiPM saturation. The saturation was simulated by considering a Poisson distribution of photons randomly hitting the pixels and counting the total number of fired pixels. The mean of the Poisson distribution was proportional to the beam input energy, giving an energy dependent saturation effect. The number of fired pixels was converted to ADC counts and then calibrated to an input energy. The simulations were integrated into the sPHENIX analysis framework.

#### VI. ANALYSIS METHODS

##### A. Data Sets

The data sets used in this analysis correspond to a beam of electrons with energies of 2, 3, 4, 6, 8, 12, 16, 20, 24 and 28 GeV. The beam was pointed at either Tower A or Tower B (see Figure 5). In this paper, whenever Tower A or Tower B is mentioned, it is referring to the corresponding data set that had the beam centered at either of those towers.

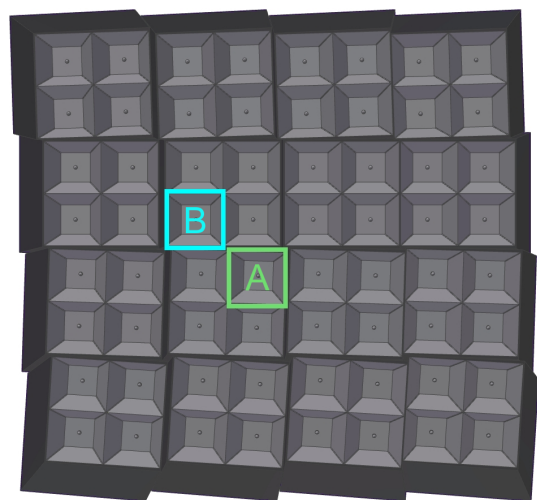


Fig. 5. Front view of the EMCal prototype showing the towers. Tower A (light green) and Tower B (light blue) are highlighted.

##### B. Electron Selection

Various cuts were used in order to suppress MIPs and hadrons, and select only events with single electrons. Single



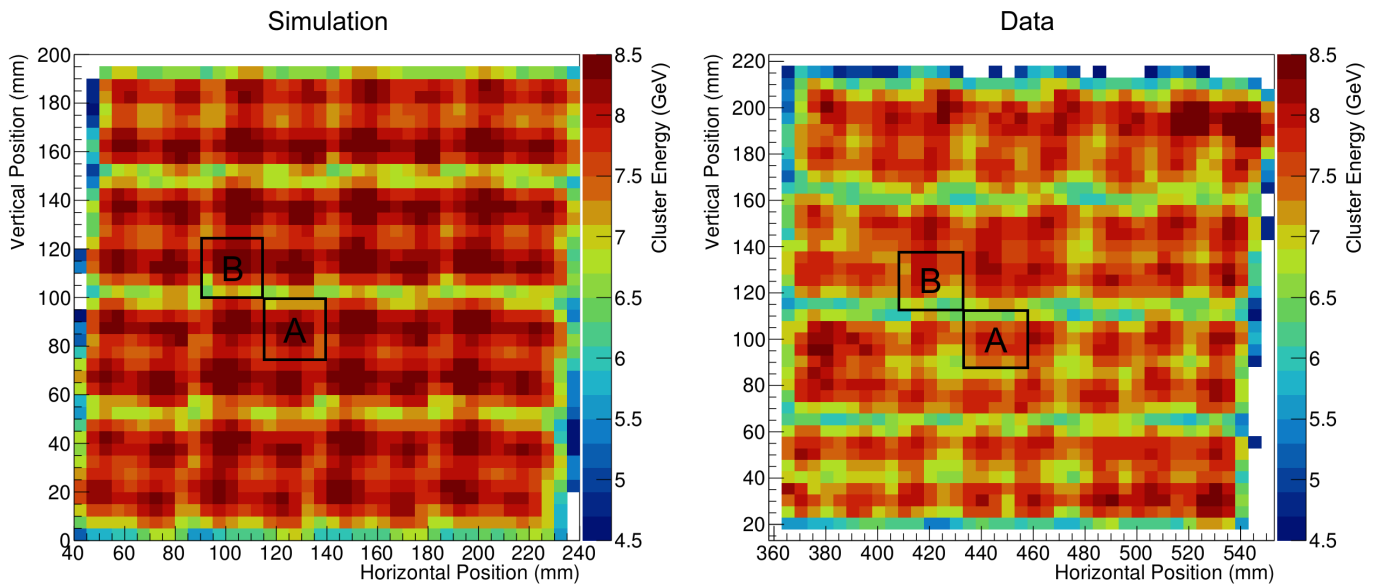


Fig. 6. Cluster Energy vs. Position for simulations (left panel) and data (right panel). The results correspond to an input energy of 8 GeV. Towers A and B are shown in black squares.

300 electrons were identified by requiring a Cherenkov cut, a  
 301 vertical and horizontal hodoscope cut, and four veto cuts. It  
 302 was generally assumed that the high energy peak in the energy  
 303 spectra of the Cherenkov counters and hodoscope channels  
 304 corresponded to the electrons. For the veto cuts, the high  
 305 energy peak was assumed to correspond to particles traveling  
 306 outside the beam position. The Cherenkov cut required the  
 307 pulse height in the Cherenkov counters to be consistent with  
 308 that of an electron. For the vertical and horizontal hodoscope  
 309 cuts, the events were required to have an energy greater than  
 310 50% of the peak energy in each hodoscope finger's energy  
 311 spectrum. Only events with one hit in the vertical and one hit  
 312 in the horizontal hodoscope fingers were considered. For the  
 313 four veto cuts, the events were required to have an energy less  
 314 than 20% of the peak energy in each veto detector's energy  
 315 spectrum. These cuts gave a number of single electrons of  
 316 approximately 5,000-50,000, depending on the energy.

### 317 C. Calibration

318 A preliminary calibration of the data, termed the *shower*  
 319 *calibration*, was performed based on how the electromagnetic  
 320 showers develop within the EMCal. A uniformity study of  
 321 the EMCal prototype showed that the energy measurements  
 322 depend on the transverse position within the EMCal. Figure  
 323 6 shows the measured energy as a function of position for  
 324 an input energy of 8 GeV, for both data and simulations. A  
 325 higher energy response was observed towards the center of  
 326 the towers than at the boundaries between the blocks and  
 327 towers. This behavior motivated the use of secondary energy  
 328 calibrations, the *position dependent correction* and the *beam*  
 329 *profile correction*.

330 The calibration procedures are as follows:

331 1) *Shower calibration*: For each event, the energy mea-  
 332 sured by the EMCal was obtained as the total energy of a

334  $5 \times 5$  cluster of towers around the maximum energy tower.  
 335 The size of the cluster was selected based on the Molière  
 336 radius for the EMCal blocks. A cluster of  $5 \times 5$  towers  
 337 contains over 95% of the electromagnetic shower energy. The energy  
 338 corresponding to a cluster of  $5 \times 5$  towers around the tower  
 339 with the maximum energy is called the *cluster energy* and  
 340 is denoted as  $E_{\text{cluster}}$ . The average cluster energy for an 8  
 341 GeV electron beam incident at the center of each tower was  
 342 reconstructed to the input energy and calibration constants  
 343 were applied tower-by-tower.

344 2) *Position dependent correction*: The energy measured  
 345 by the EMCal was corrected by a constant that depends on  
 346 the position of the hit in the EMCal. Two different correc-  
 347 tions were obtained, the difference lying in the availability  
 348 of external position information. In the first, the position  
 349 was determined by a horizontal and a vertical hodoscope  
 350 finger, with a total of  $8 \times 8$  possible positions. In the second,  
 351 the position was determined by the energy averaged cluster  
 352 position measured by the EMCal, discretized in  $8 \times 8$  bins that  
 353 matched the hodoscope. The position dependent calibration  
 354 constants were obtained from 8 GeV data as described below.  
 355 The procedure is the same for both the hodoscope-based and  
 356 cluster-based corrections. For each of the 64 possible position  
 357 bins, a histogram was filled with the cluster energy in that  
 358 position. The histogram was then fit with a Gaussian of mean  
 359  $\mu$ . The calibration constant for each position was obtained as  
 360  $8 \text{ GeV}/\mu$ . The position dependent correction improved the  
 361 energy resolution by 2-3%, depending on the energy.

362 The sPHENIX tracker can be used in place of a hodoscope  
 363 to develop a position dependent correction. Since the tracker  
 364 is only sensitive to charged particles, the cluster-based  
 365 correction can be used for neutral particles instead.

366 3) *Beam profile correction*: In the experiment, the beam  
 367 had a different transverse profile at different energies. In  
 368

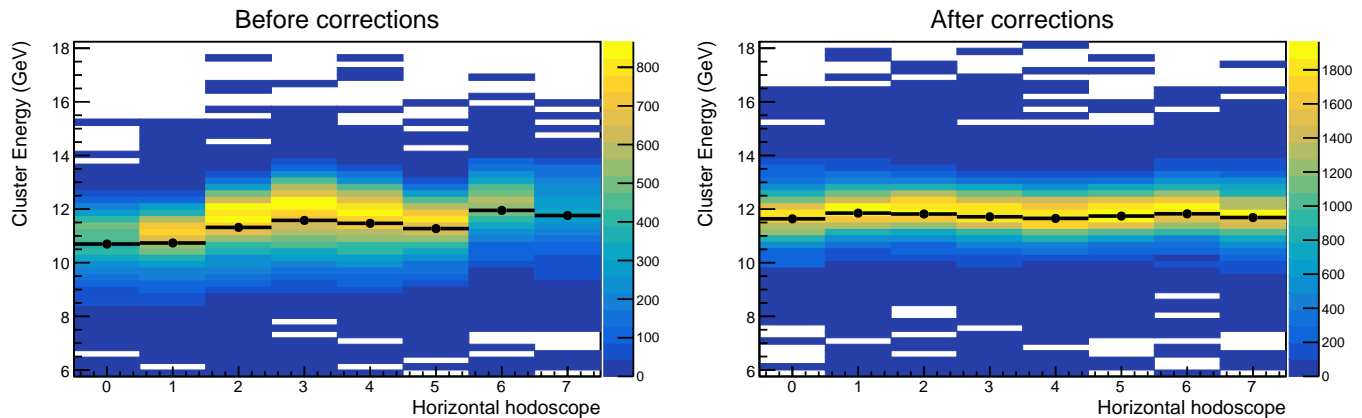


Fig. 7. Cluster Energy vs. Horizontal Hodoscope Position before (left panel) and after (right panel) applying the hodoscope-based position dependent correction and the beam profile correction. The color scale represents the number of events, while the black points correspond to the mean of the energy distributions for each hodoscope position. The data corresponds to a 12 GeV beam centered at Tower A.

369 addition to the position dependent correction, a *beam profile*  
 370 *correction* was introduced in order to correct for the energy  
 371 dependence of the beam profile. This correction consisted of  
 372 filling the energy histograms with weights that were obtained  
 373 by making the distribution of beam particles uniform as a  
 374 function of position. The beam profile correction changed the  
 375 energy resolution by 0.1-0.5%, depending on the energy.

376 The effects of these corrections on the energy response can  
 377 be seen in Figure 7. This figure shows the cluster energy  
 378 as a function of horizontal hodoscope position. The data is  
 379 shown before and after applying the hodoscope-based position  
 380 dependent correction and the beam profile correction. After  
 381 the corrections are applied, the energy response of the EMCAL  
 382 becomes more uniform.

383 The simulations also included the position dependent and  
 384 beam profile corrections. The corrections were obtained using  
 385 the procedure previously described, where the simulated  
 386 position was discretized in  $8 \times 8$  bins to mock the hodoscope.

## 387 VII. RESULTS AND DISCUSSION

388 Following the analysis procedure described in the previous  
 389 section, the energy resolution and linearity of the EMCAL  
 390 prototype was obtained for input energies ranging from 2 to  
 391 28 GeV, for both simulations and data.

392 Figure 8 shows the energy resolution and linearity of the  
 393 EMCAL prototype using a  $2.5 \times 2.5 \text{ cm}^2$  cut centered at the  
 394 tower. The  $2.5 \times 2.5 \text{ cm}^2$  cut was selected based on the  
 395 approximate area of a tower. The results are shown for data and  
 396 simulations and include all corrections. The uncertainty bars  
 397 on the data points correspond to the statistical uncertainties.  
 398 The linearity was obtained as  $E_{\text{cluster}} = E + cE^2$ , where  $E$   
 399 is the input energy and  $c$  is a constant. The resolution was  
 400 obtained as  $\sigma(E_{\text{cluster}})/\langle E_{\text{cluster}} \rangle = \delta p/p \oplus a \oplus b/\sqrt{E}$ , where  
 401  $a$  and  $b$  are constants, and a  $\delta p/p = 2\%$  term was added to  
 402 account for the beam momentum spread. Table II shows the  
 403 values of the fit constants  $a$ ,  $b$ , and  $c$ .

404 The resolution obtained with the cluster-based correction  
 405 differs from the hodoscope-based correction by approximately  
 406 0.6% in the constant term and 2.1% in the  $1/\sqrt{E}$  term. Since

TABLE II  
 EMCAL ENERGY LINEARITY AND RESOLUTION FOR A  $2.5 \times 2.5 \text{ cm}^2$   
 CUT CENTERED ON A TOWER

$$\text{Resolution fit: } \sigma(E_{\text{cluster}})/\langle E_{\text{cluster}} \rangle = 2\% \oplus a \oplus b/\sqrt{E}$$

$$\text{Linearity fit: } E_{\text{cluster}} = E + cE^2$$

	Tower	$a$ (%)	$b$ (% $\text{GeV}^{1/2}$ )	$c$ ( $\text{GeV}^{-1}$ )
Data, hodoscope	A	$3.2 \pm 0.1$	$13.8 \pm 0.2$	$(-9.4 \pm 0.1) \times 10^{-4}$
Data, hodoscope	B	$3.8 \pm 0.1$	$12.8 \pm 0.2$	$(-10.9 \pm 0.1) \times 10^{-4}$
Data, cluster	A	$2.7 \pm 0.1$	$15.8 \pm 0.3$	$(-12.8 \pm 0.2) \times 10^{-4}$
Data, cluster	B	$3.2 \pm 0.1$	$14.9 \pm 0.3$	$(-8.6 \pm 0.3) \times 10^{-4}$
Simulation		$3.04 \pm 0.05$	$12.6 \pm 0.1$	$(-9.3 \pm 0.1) \times 10^{-4}$

407 the cluster-based correction depends on the position measured  
 408 by the EMCAL itself and not the hodoscope, the difference  
 409 in the results can potentially arise from the reduced cluster  
 410 position resolution of the EMCAL at lower energy. Additionally,  
 411 the energy resolution seems to be better in the simulations than  
 412 in the hodoscope corrected data by approximately 0.5% in the  
 413 constant term and 0.7% in the  $1/\sqrt{E}$  term. These differences  
 414 can arise from the lower energy collection efficiency at the  
 415 boundaries between towers and blocks, as well as tower by  
 416 tower variations that are not present in the simulations. The  
 417 differences in the resolution results can be minimized by  
 418 making a cut at the center of the towers, where the energy  
 419 collection is most efficient. Figure 9 shows the linearity and  
 420 resolution results using a  $1.0 \times 0.5 \text{ cm}^2$  cut at the center of the  
 421 towers. This figure shows better agreement between data and  
 422 simulations. Table III shows the corresponding linearity and  
 423 resolution fit constants.

424 Additionally, Figure 8 shows that for energies below 15 GeV  
 425 the energy resolution for Towers A and B generally agree  
 426 within the statistical uncertainties, while for higher energies  
 427 the resolution is consistently larger for Tower B than for  
 428 Tower A. The disagreement between the resolution of the

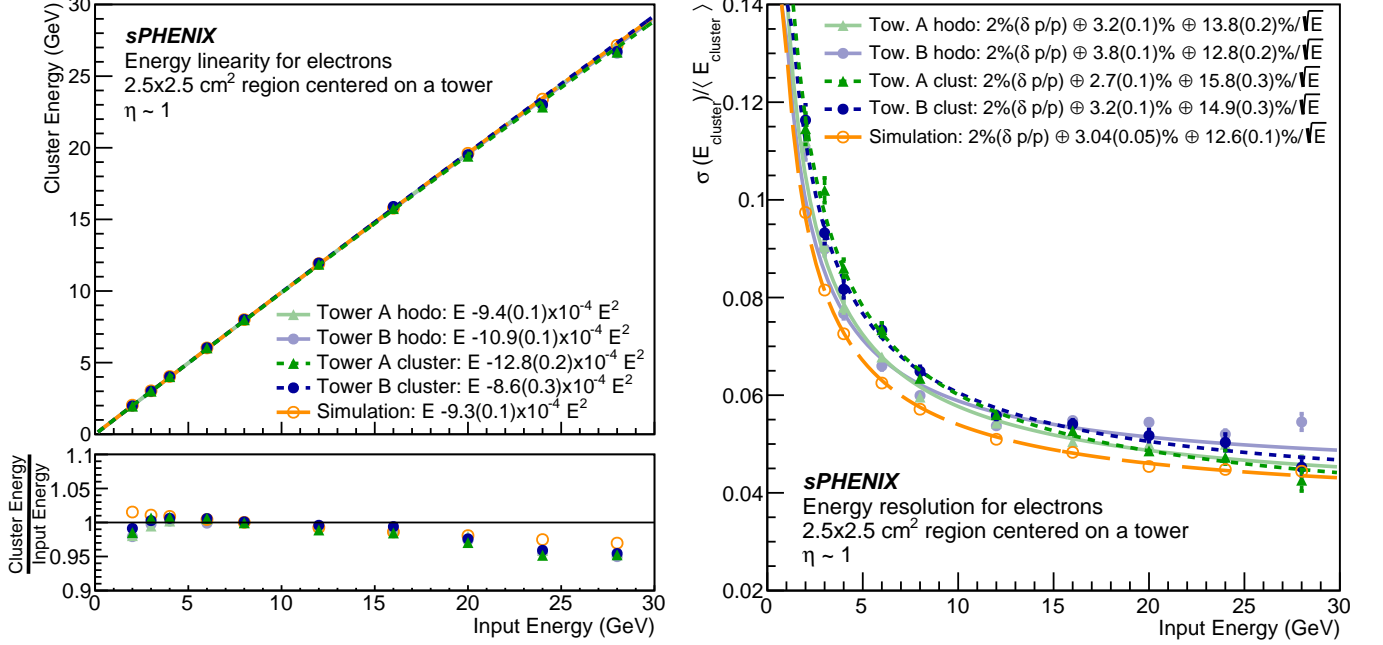


Fig. 8. Linearity and resolution of the EMCal prototype for a  $2.5 \times 2.5 \text{ cm}^2$  centered on a tower. The  $2.5 \times 2.5 \text{ cm}^2$  cut was selected based on the approximate area of a tower. The data corresponds to Tower A (green triangles) and Tower B (purple full circles). The data was corrected using the hodoscope-based (solid lines) and cluster-based (fine dashed lines) position dependent corrections, as well as the beam profile correction. Simulations (orange open circles, coarse dashed line) are shown for comparison and include the same corrections as the data. (top left panel) Cluster Energy vs. Input Energy. (bottom left panel)  $\frac{\text{Cluster Energy}}{\text{Input Energy}}$  vs. Input Energy. The linearity was obtained as  $E_{\text{cluster}} = E + cE^2$ . (right panel) Energy Resolution vs. Input Energy. The resolution was obtained as  $\sigma(E_{\text{cluster}})/\langle E_{\text{cluster}} \rangle = \delta p/p \oplus a \oplus b/\sqrt{E}$ , where a  $\delta p/p = 2\%$  term was added to account for the beam momentum spread.

429 towers above 15 GeV is observed for both the hodoscope-  
430 based and cluster-based results of Figure 8 and contributes to  
431 the fit constants of Table II. However, this disagreement is not  
432 observed when a cut at the center of the towers is used, as  
433 shown in Figure 9 and Table III.

TABLE III

EMCAL ENERGY LINEARITY AND RESOLUTION FOR A  $1.0 \times 0.5 \text{ cm}^2$   
CUT AT THE CENTER OF A TOWER

Resolution fit:  $\sigma(E_{\text{cluster}})/\langle E_{\text{cluster}} \rangle = 2\% \oplus a \oplus b/\sqrt{E}$

Linearity fit:  $E_{\text{cluster}} = E + cE^2$

	Tower	$a$ (%)	$b$ ( $\% \text{ GeV}^{1/2}$ )	$c$ ( $\text{GeV}^{-1}$ )
Data, hodoscope	A	$2.4 \pm 0.2$	$12.3 \pm 0.5$	$(-12.9 \pm 0.3) \times 10^{-4}$
Data, hodoscope	B	$2.3 \pm 0.2$	$13.4 \pm 0.5$	$(+0.7 \pm 0.3) \times 10^{-4}$
Data, cluster	A	$2.4 \pm 0.2$	$13.2 \pm 0.5$	$(-10.9 \pm 0.3) \times 10^{-4}$
Data, cluster	B	$2.7 \pm 0.2$	$12.8 \pm 0.4$	$(-5.9 \pm 0.3) \times 10^{-4}$
Simulation		$2.6 \pm 0.2$	$11.9 \pm 0.3$	$(-9.1 \pm 0.3) \times 10^{-4}$

434 Comparing the 2018 results to the 2016 results of reference  
435 [9], the resolution improved for energies in the range 2 to 8  
436 GeV. In terms of the resolution fit, the  $1/\sqrt{E}$  term of the reso-  
437 lution decreased by approximately 2.5% and the constant term  
438 increased by approximately 0.7%. Furthermore, the linearity

improved by approximately 1% in the 2018 prototype with  
respect to the 2016 prototype.

## VIII. CONCLUSIONS

A 2D projective prototype of the sPHENIX EMCal was  
constructed and tested. The EMCal prototype's energy re-  
sponse to electrons was studied as a function of incident  
position and energy. The energy resolution and linearity of the  
EMCal prototype were obtained using two different position  
dependent energy corrections (hodoscope-based and cluster-  
based) as well as a beam profile correction. The two data  
sets used in this analysis had beam energies ranging from  
2 to 28 GeV, but one had the beam centered at Tower A  
and the other one had the beam centered at Tower B. The  
energy resolution was obtained for each tower using a cut  
of  $2.5 \times 2.5 \text{ cm}^2$  centered on the tower. Based on the ho-  
doscope position dependent correction, the EMCal prototype  
was found to have a tower averaged energy resolution of  
 $\sigma(E)/\langle E \rangle = 3.5(0.1) \oplus 13.3(0.2)/\sqrt{E}$ . Based on the cluster  
position dependent correction, the tower averaged resolution  
was found to be  $\sigma(E)/\langle E \rangle = 3.0(0.1) \oplus 15.4(0.3)/\sqrt{E}$ .  
These energy resolution results meet the requirements of the  
sPHENIX physics program.

## ACKNOWLEDGMENTS

This research was carried out using resources from the  
Fermi National Accelerator Laboratory (Fermilab), a HEP user



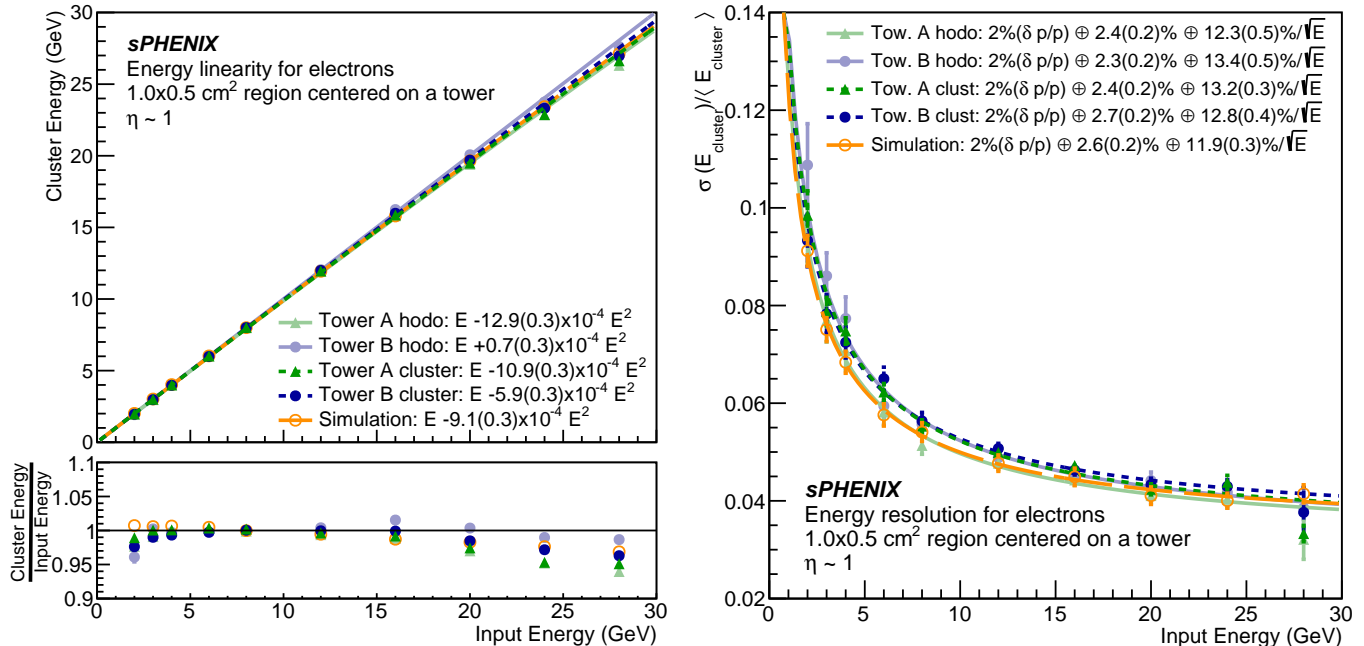


Fig. 9. Linearity and resolution of the EMCal prototype for a  $1.0 \times 0.5 \text{ cm}^2$  cut at the center of a tower. The data corresponds to Tower A (green triangles) and Tower B (purple full circles). The data was corrected using the hodoscope-based (solid lines) and cluster-based (fine dashed lines) position dependent corrections, as well as the beam profile correction. Simulations (orange open circles, coarse dashed line) are shown for comparison and include the same corrections as the data. (top left panel) Cluster Energy vs. Input Energy. (bottom left panel)  $\frac{\text{Cluster Energy}}{\text{Input Energy}}$  vs. Input Energy. The linearity was obtained as  $E_{\text{cluster}} = E + cE^2$ . (right panel) Energy Resolution vs. Input Energy. The resolution was obtained as  $\sigma(E_{\text{cluster}})/\langle E_{\text{cluster}} \rangle = \delta p/p \oplus a \oplus b/\sqrt{E}$ , where a  $\delta p/p = 2\%$  term was added to account for the beam momentum spread.

464 facility managed by the Fermi Research Alliance, LLC, for the  
 465 U.S. Department of Energy, Office of Science, acting under  
 466 Contract No. DE-AC02-07CH11359. The authors would like  
 467 to thank the technical staffs of the University of Illinois at  
 468 Urbana-Champaign and Brookhaven National Laboratory for  
 469 assisting the construction of the electromagnetic calorimeter  
 470 prototype. The authors would also like to thank Dr. O. Tsai  
 471 for providing the hodoscope used in the beam test.

472 C.A. Aidala, E.A. Gamez, N.A. Lewis and J.D. Osborn are  
 473 with the Department of Physics at the University of Michigan,  
 474 Ann Arbor, MI 48109-1040.

475 S. Altaf, M. Phipps, C. Riedl, T. Rinn, A.C. Romero Her-  
 476 nandez, A.M. Sickles, E. Thorsland and X. Wang are with the  
 477 Department of Physics at the University of Illinois Urbana-  
 478 Champaign, Urbana, IL 61801-3003.

479 R. Belmont is with the Department of Physics at the  
 480 University of Colorado Boulder, Boulder, CO 80309-0390 and  
 481 the Department of Physics and Astronomy at the University  
 482 of North Carolina Greensboro, Greensboro, NC 27402-6170.

483 S. Boose, D. Cacace, E. Desmond, J.S. Haggerty, J. Huang,  
 484 M.D Lenz, W. Lenz, E.J. Mannel, R. Pisani, S. Polizzo,  
 485 M. Purschke, S. Stoll, and C.L. Woody are with Brookhaven  
 486 National Laboratory, Upton, NY 11973-5000.

487 M. Connors is with the Department of Physics and Astron-  
 488 omy at the Georgia State University, Atlanta, GA 30302-5060  
 489 and the RIKEN BNL Research Center, Upton, NY 11973-  
 490 5000.

J. Frantz and A. Pun are with the Department of Physics  
 and Astronomy at Ohio University, Athens, OH 45701-6817.

N. Grau is with the Department of Physics at Augustana  
 University, Sioux Falls, SD 57197.

A. Hodges, M. Sarsour and X. Sun are with the Department  
 of Physics and Astronomy at the Georgia State University,  
 Atlanta, GA 30302-5060.

Y. Kim is with the Department of Physics at the University  
 of Illinois Urbana-Champaign, Urbana, IL 61801-3003 and the  
 Department of Physics and Astronomy at Sejong University,  
 Seoul 05006, Korea.

D.V. Perepelitsa, C. Smith, and F. Vassalli are with the  
 Department of Physics at the University of Colorado Boulder,  
 Boulder, CO 80309-0390.

Z. Shi is with the Department of Physics at the Mas-  
 sachusetts Institute of Technology, Cambridge, MA 02139-  
 4307.

## REFERENCES

- [1] A. Adare *et al.*, "An Upgrade Proposal from the PHENIX Collabora-  
tion," *arXiv:1501.06197*, 2015.
- [2] E.-C. Aschenauer *et al.*, "The RHIC Cold QCD Plan for 2017 to 2023:  
A Portal to the EIC," 2016.
- [3] K. Adcox *et al.*, "Formation of dense partonic matter in relativistic  
nucleus nucleus collisions at RHIC: experimental evaluation by the  
PHENIX collaboration," *Nucl. Phys.*, vol. A757, pp. 184–283, 2005.
- [4] J. Adams *et al.*, "Experimental and theoretical challenges in the search  
for the quark gluon plasma: the STAR collaboration's critical assessment  
of the evidence from RHIC collisions," *Nucl. Phys.*, vol. A757, pp. 102–  
183, 2005.

- 520 [5] B. B. Back *et al.*, “The PHOBOS perspective on discoveries at RHIC,”  
521 *Nucl. Phys.*, vol. A757, pp. 28–101, 2005.
- 522 [6] I. Arsene *et al.*, “Quark gluon plasma and color glass condensate at  
523 RHIC? The perspective from the BRAHMS experiment,” *Nucl. Phys.*,  
524 vol. A757, pp. 1–27, 2005.
- 525 [7] T. G. O’Connor *et al.*, “Design and testing of the 1.5 T superconducting  
526 solenoid for the BaBar detector at PEP-II in SLAC,” *IEEE Trans. Appl.*  
527 *Supercond.*, vol. 9, pp. 847–851, 1999.
- 528 [8] The sPHENIX Collaboration, “sPHENIX Technical Design Report,  
529 PD-2/3 Release,” [https://indico.bnl.gov/event/7081/attachments/25527/](https://indico.bnl.gov/event/7081/attachments/25527/38284/sphenix_tdr_20190513.pdf)  
530 [38284/sphenix\\_tdr\\_20190513.pdf](https://indico.bnl.gov/event/7081/attachments/25527/38284/sphenix_tdr_20190513.pdf), 2019.
- 531 [9] C. A. Aidala *et al.*, “Design and Beam Test Results for the sPHENIX  
532 Electromagnetic and Hadronic Calorimeter Prototypes,” *IEEE Trans.*  
533 *Nucl. Sci.*, vol. 65, no. 12, pp. 2901–2919, 2018.
- 534 [10] O. Tsai, L. Dunkelberger, C. Gagliardi, S. Heppelmann, H. Huang  
535 *et al.*, “Results of R&D on a new construction technique for W/ScFi  
536 Calorimeters,” *J. Phys. Conf. Ser.*, vol. 404, p. 012023, 2012.
- 537 [11] O. D. Tsai *et al.*, “Development of a forward calorimeter system for  
538 the STAR experiment,” *J. Phys. Conf. Ser.*, vol. 587, no. 1, p. 012053,  
539 2015.
- 540 [12] B. D. Leverington *et al.*, “Performance of the prototype module of the  
541 GlueX electromagnetic barrel calorimeter,” *Nucl. Instrum. Meth.*, vol.  
542 A596, pp. 327–337, 2008.
- 543 [13] S. A. Sedykh *et al.*, “Electromagnetic calorimeters for the BNL muon  
544 (g-2) experiment,” *Nucl. Instrum. Meth.*, vol. A455, pp. 346–360, 2000.
- 545 [14] T. Armstrong *et al.*, “The E864 lead-scintillating fiber hadronic calorime-  
546 ter,” *Nucl. Instrum. Meth.*, vol. A406, pp. 227–258, 1998.
- 547 [15] R. D. Appuhn *et al.*, “The H1 lead / scintillating fiber calorimeter,” *Nucl.*  
548 *Instrum. Meth.*, vol. A386, pp. 397–408, 1997.
- 549 [16] D. W. Hertzog, P. T. Debevec, R. A. Eisenstein, M. A. Graham, S. A.  
550 Hughes, P. E. Reimer, and R. L. Tayloe, “A high resolution lead  
551 scintillating fiber electromagnetic calorimeter,” *Nucl. Instrum. Meth.*,  
552 vol. A294, pp. 446–458, 1990.
- 553 [17] W. Anderson *et al.*, “Design, Construction, Operation and Performance  
554 of a Hadron Blind Detector for the PHENIX Experiment,” *Nucl. In-*  
555 *strum. Meth.*, vol. A646, p. 35, 2011.
- 556 [18] M. L. Purschke, “RCDAQ, a lightweight yet powerful data acquisition  
557 system,” <https://github.com/sPHENIX-Collaboration/rcdaq>, 2012.
- 558 [19] M. L. Purschke, “RCDAQ, a lightweight yet powerful data acqui-  
559 sition system,” [http://www.phenix.bnl.gov/~purschke/rcdaq/rcdaq\\_doc.](http://www.phenix.bnl.gov/~purschke/rcdaq/rcdaq_doc.pdf)  
560 [pdf](http://www.phenix.bnl.gov/~purschke/rcdaq/rcdaq_doc.pdf), 2012.
- 561 [20] The Fermilab test beam facility. accessed: Apr 5, 2017. [Online].  
562 Available: <http://ftbf.fnal.gov>
- 563 [21] N. Feege, “Low-energetic hadron interactions in a highly granular  
564 calorimeter,” Ph.D. dissertation, Physics Department, Hamburg U.,  
565 2011. [Online]. Available: [http://www-library.desy.de/cgi-bin/showprep.](http://www-library.desy.de/cgi-bin/showprep.pl?thesis11-048)  
566 [pl?thesis11-048](http://www-library.desy.de/cgi-bin/showprep.pl?thesis11-048)
- 567 [22] M. Blatnik *et al.*, “Performance of a Quintuple-GEM Based RICH  
568 Detector Prototype,” *IEEE Trans. Nucl. Sci.*, vol. 62, no. 6, pp. 3256–  
569 3264, 2015.
- 570 [23] M. Backfish, “Meson test beam momentum selection,” [http://beamdocs.](http://beamdocs.fnal.gov/AD/DocDB/0048/004831/004/DPOverP.pdf)  
571 [fnal.gov/AD/DocDB/0048/004831/004/DPOverP.pdf](http://beamdocs.fnal.gov/AD/DocDB/0048/004831/004/DPOverP.pdf), 2016.
- 572 [24] S. Agostinelli *et al.*, “GEANT4: A Simulation toolkit,” *Nucl. In-*  
573 *strum. Meth.*, vol. A506, pp. 250–303, 2003.
- 574 [25] J. Allison *et al.*, “Geant4 developments and applications,” *IEEE Trans.*  
575 *Nucl. Sci.*, vol. 53, p. 270, 2006.
- 576 [26] J. B. Birks, “Scintillations from Organic Crystals: Specific Fluorescence  
577 and Relative Response to Different Radiations,” *Proc. Phys. Soc.*, vol.  
578 A64, pp. 874–877, 1951.
- 579 [27] M. Hirschberg, R. Beckmann, U. Brandenburg, H. Brueckmann, and  
580 K. Wick, “Precise measurement of Birks  $k_B$  parameter in plastic  
581 scintillators,” *IEEE Trans. Nucl. Sci.*, vol. 39, pp. 511–514, 1992.